ARTICLE   OPEN

Room temperature photosensitive ferromagnetic semiconductor using MoS$_2$

Jingjing Lu[1], Yan Xu[2], Jingsong Cui[2], Peng Zhang[1], Chenxi Zhou[2], Hanuman Singh[3], Shuai Zhang[2], Long You[2] and Jeongmin Hong[1,3 ✉]

Two-dimensional semiconductors, including transition metal dichalcogenides (TMDs), are of interest in electronics and photonics but remain nonmagnetic in their intrinsic form. Atomic modulation using physical and chemical ways is an effective means to control the physical properties such as magnetic and electrical properties of two-dimensional materials which can be controlled by irradiation. Here we treat mechanically exfoliated MoS$_2$ with a helium ion beam, which exhibits semiconducting and ferromagnetic ordering at room temperature, while Monte Carlo simulations and theoretical calculations confirmed that the control of nanoholes result in the presence of magnetism. In addition, the irradiation results of multilayer MoS$_2$ show that the magnetic moment increases with the increase of 10 layers. The conductivity remains virtually unchanged before and after being treated by a helium ion beam. The treated MoS$_2$ spintronic device displays the switch of 'on/off' under the light, magnetic field, and/or electric field, which means 2D photosensitive ferromagnetic semiconductor functions are successfully demonstrated at room temperature.

INTRODUCTION

With the transistor gate thickness scaled to the sub-10-nm range, exponentially increasing charge leakage makes it difficult to further advance silicon semiconductor technologies[1–3]. In contrast, spintronic devices that exploit not only the charge but also the magnetic spin of the electron have the potential to be scaled to the sub-1-nm range[3–5]. Moreover, spintronics promise to give birth to a new breed of computing devices with important advantages such as nonvolatility, data densities above 100 terabit/in[2], data rates in the terahertz range, and negligibly low power consumption[4–7]. However, to enable many potential groundbreaking applications, a new material that combines both magnetic and semiconducting properties at room temperature needs to be discovered. Two-dimensional (2D) magnetic and semiconducting materials have been considered to be promising candidates for applications in next-generation spintronic devices due to their high carrier mobility, broad coverage of their adjustable band gaps, and high flexibility[8–10].

Recent discoveries on van der Waals 2D magnetism are based on well-known magnetic insulators such as CrI$_3$, X$_2$(X=Fe, Cr, etc.) Ge$_2$Te$_6$, X(X=Fe, Mn, etc.)PS$_3$, and many other compounds[11–23]. CrI$_3$ and other halide insulators exhibit magnetic ordering only at low temperatures and easy oxidation, which are major bottlenecks to their actual application in electronic devices[11–16]. Fe$_2$Ge$_2$Te$_6$ and other Ge-Te-based compounds materials have no energy gap and no photosensitive[17–19]. FePS$_3$ and other P-S-based compounds show low-temperature antiferromagenetic[20–23]. The effects of 2D magnetism are systematic and significant, but room-temperature semiconducting ferromagnetism in 2D materials remains a major open question.

The class of hexagonal transition metal dichalcogenides (*h*-TMDs) shows direct and indirect band gap semiconducting behavior with spin splitting at the valence band maximum, thereby showing promise to manipulate the spin degree of freedom and valley polarization[20]. Moreover, with its extreme dimensional confinement, tightly bound excitons, and strong electron–electron interactions due to weak screening, *h*-TMDs has been revealed as an ideal low-dimensional compound for exploring many interesting quantum phenomena, such as spin and valley Hall effects, ferromagnetism, and superconductivity[24–29]. Additionally, *h*-TMDs have fascinating optical properties, including its strong band gap photoluminescence at the edge, and surface-sensitive luminescence. and strain–controlled optical band gap[30–36]. However, most of the intrinsic TMDs are nonmagnetic at ambient condition. Some TMDs are doped by Fe, V, Mn, etc, as the room temperature dilute ferromagnetic semiconductors, which often destroys its semiconductivity[37–42]. As a member of TMDs, monolayer MoS$_2$ has three atomic layers with a center layer of molybdenum (*Mo*) around sulfur (*S*) layers on both sides. The states near the band gap are well known to be mainly from the *d*-orbitals of Mo[43]. A thick layer of MoS$_2$ exhibits the characteristics of an indirect-gap semiconductor, whereas a monolayer of MoS$_2$ is a direct-gap semiconductor with an energy of 1.8 eV[44]. Recently, many studies have reported using monolayer and few-layer MoS$_2$, which have been shown to display unprecedented electronic properties, such as room-temperature ballistic transport and quantum conductance[45–48] Furthermore, theoretical calculations indicate that a treated MoS$_2$ sheet is likely to be simultaneously semiconducting and magnetic; in other words, it acts as a room-temperature ferromagnetic semiconductor. The pristine MoS$_2$ monolayer has the photosensitive properties closely related to the direct gap and the excitons and strong electron-electron interactions, which could control magnetic and semiconducting behavior simultaneously. That means ultrafast laser pulses induced ferromagnetic semiconductor promise the fastest and most energy efficient means of manipulating electron spin devices.

However, it is still challenging to conduct a thorough experimental study on such small samples to understand the magnetic properties of the new material using volume- and surface-averaged magnetometry. Here, we prove that a treated form of MoS$_2$ can be turned into a room-temperature

[1]School of Sciences, Hubei University of Technology, Wuhan, China. [2]School of Optical and Electronic Information, Huazhong University of Science and Technology, Wuhan, China. [3]EECS, UC Berkeley, Berkeley, CA, USA. ✉email: jehong@berkeley.edu
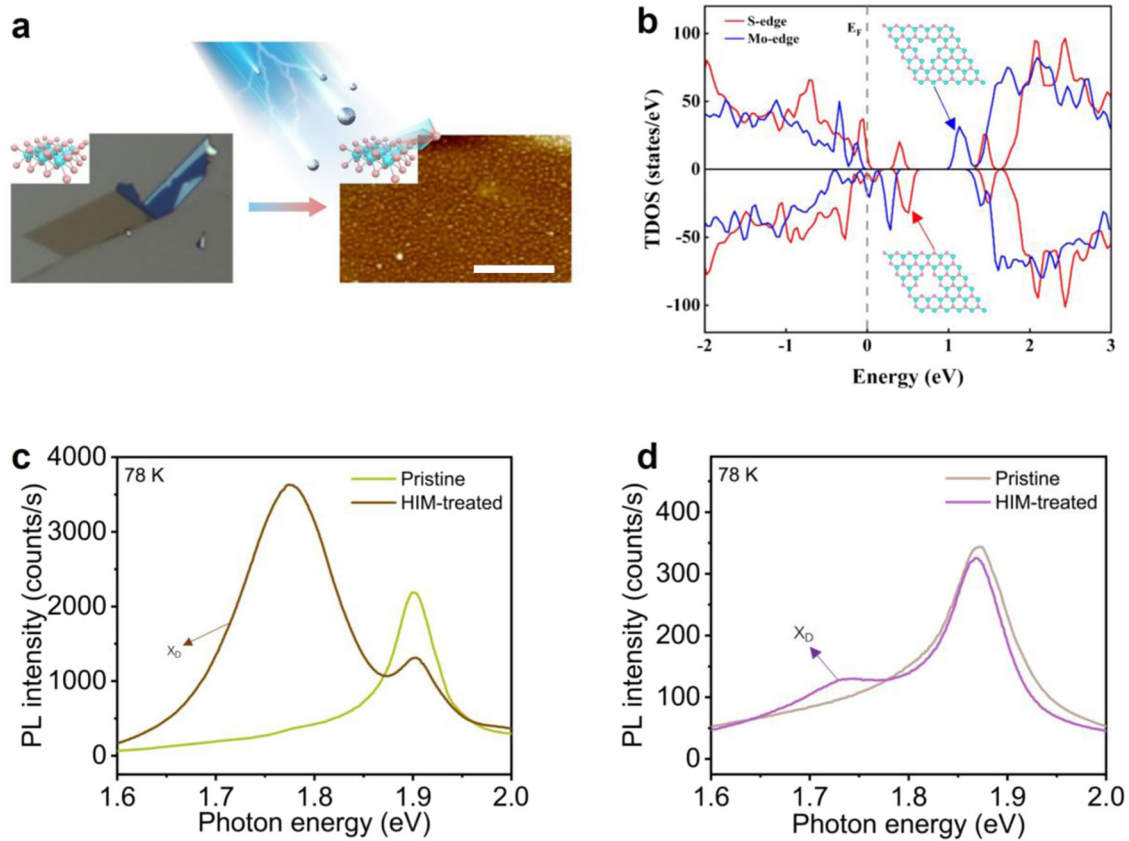
Fig. 1 Schematics of the structures and the related characteristics before and after the treatment. a Before and after the HIM of the exfoliated MoS_2. A pristine MoS_2 sample was treated with helium ions, causing the loss of S atoms and Mo atoms, resulting in the nanoholes shown as the white dots in right. The scale bar is 1 um. **b** Theoretical calculations of the TDOS at the S-edge (red line) and Mo-edge (blue line) nanoholes. The inset shows the structures of each edge. TDOS shows a bandgap of approximately 0.7 eV and asymmetry at the Fermi level. PL spectra of the monolayer **c** and multilayer (5 layers) **d** of MoS_2 samples at 78 K.

photosensitive magnetic semiconductor by experimental and theoretical studies. Another challenge is to control the magnetic and electronic properties of MoS_2 via the modulation of vacancies through gentle ion treatment. Helium ion milling (HIM) can make it possible to gently generate selective vacancies as a part of physical approaches[49–51]. Chemical modulation will be possible, but there is a limitation to having layer-by-layer vacancies and/or chemisorption. Through device measurements, the system is realized as a reliable ferromagnetic semiconductor device. The present experimental study aims to shed light on the origin of magnetism in treated 2D materials.

RESULTS

The exfoliated MoS_2 treated by a helium ion beam

Figure 1a shows a monolayer of MoS_2 and the model of the MoS_2 structure which is exfoliated in a large area (~ 20 to 30 µm, which is smaller than the area of 40–50 µm², and is whole inside the helium ion irradiation area). It should be noted that even the 'pristine' stage has long-range line vacancies and clusters and consists of crystalline regions with characteristic lengths on the order of a few microns. Then, a helium ion beam is applied to the basal plane of the sample surface. As shown in Fig. 1a, the overall process of helium ion irradiation was described. Above the sample, helium ions bombard and collide with S and Mo atoms on the surface of the sample. The ordered nanoholes are generated compared with the pristine dots. In the helium ion-treated area, S atoms are selectively removed and brings the generation of S vacancies[21,37,38]. Thus, white dots are produced after S and Mo in a

region disappear (nanoholes) in the right graph of Fig. 1a. The AFM/STM images by the different dosages are shown in Fig S7 and the nanoholes are characterized directly with the size of (1–4 nm²). Monte Carlo simulations were performed to estimate the vacancy distribution with different helium ion energies and in different layers. The results are also shown in Figs. S1, S2, and S3, respectively. Figure S1, it predicts a decreasing tendency of vacancy number with increasing helium ion energy. Besides, vacancies on monolayer distribute very uniform, which implies that an ion beam with defined parameters can bring in a uniform density of vacancies, that is, the controllable engineer on defects of MoS_2 can be achieved. In Fig. S2, we found that vacancy density increases rapidly as depth increases, this implies that in multilayers samples, the deeper layer of MoS_2 will have more vacancies. As shown in Fig. S3, we calculated a model of 20 layers MoS_2 and got its vacancy density with different layers. The results show the population of the vacancies does increase almost linearly until nearly constant when the layer increases to more than 10. The nanoholes were investigated and calculated, which affects the electrical and magnetic properties of layered MoS_2.

We considered two representative nanohole vacancy structures, V_{S-edge} and $V_{Mo-edge}$, as shown in the inset of Fig. 1b. Due to the Mo and S-edge nanoholes, the valence band shown in the TDOS of Fig. 1b increases to various maximums compared to the pristine case as also described in Fig. S4 and the energy gap decreases. The results indicate that the nanoholes of the specific shapes will cause a single layer of MoS_2 to have behavior that is similar to p-doping. The principle of magnetism caused by nanohole

vacancy will be explained in detail in the Magnetic Properties of MoS₂ section.

At low temperatures, monolayer MoS₂ shows PL peaks at 1.78 eV and 1.91 eV, respectively (Fig. 1c). The charged to neutral exciton transition is associated with charge depletion or localization, which stabilizes or destabilizes neutral or charged excitons. Excitons bound to vacancies lead to light emission at energies lower than the band-to-band optical transition energy. Such interactions become stronger in reduced dimensionalities due to tighter localization of the electron. The peak at 1.78 eV appears after irradiation, and its intensity increases at higher doses; we attribute it to the radiative recombination of bound excitons (X_b) and neutral excitons (X_0) bound to vacancies. The peak appears stronger and broader than in the HIM-treated samples due to a higher density of vacancies and clusters.

Low-temperature PL spectra clearly show the difference between the pristine and treated monolayers, as shown in Fig. 1c, d. They represent monolayers and multilayers with an S vacancy yield that has an even stronger PL intensity. The emergence of the bound peak (X_b or X_D) in the PL spectra for both monolayer and multilayer MoS₂ is attributed to the introduction of vacancies by the helium ion dose. Since X_b is associated with excitons bound to vacancies, the PL intensity of X_b is expected to saturate at high excitation power intensities when these vacancies are fully populated with excitons due to the loss and/or emission of energy by electron-hole pairs. The X_D peak is prominent at low temperatures or low excitation powers, as described in Fig. S5. Then, it becomes weaker as the temperature is increased and completely disappears at room temperature. Both pristine and treated monolayers exhibit high optical quality with a strong, single PL peak associated with the band-to-band optical transition at the K point.

As shown in Fig. 1d, the PL results show the multilayer sample (5 L) before and after HIM treatment and the appearance of S vacancies. After treatment, the result implies semiconducting behavior due to the disorder of the MoS₂ crystal structures. The layer dependence of the PL spectra confirms that the HIM treatment is uniform through the layers. After treatment, the full-width-at-half maximum (FWHM) of the Raman peaks broadens due to relaxation of the Raman selection rule as shown in Fig. S7.

Fig. S6 describes the comprehensive measurements of samples with different thicknesses due to different HIM doses. The PL peaks can be modulated layer by layer, i.e., monolayer, multilayer, thin layer, and thick layers, by using a different HIM dose. In the case of a monolayer, the X_D peaks shift with an increasing HIM dose. Eventually, the peak disappears after reaching a state dominated by vacancies, in other words, physical defect states. Multilayers can be formed by changing the irradiation dose. The main PL peak at around 1.90 eV increases by 3 times, while the PL peak position shifts to a higher energy. The energy level could be controllable.

From the PL measurements, MoS₂ monolayer is a semiconductor with a direct bandgap of 1.8 eV with vacancy states. In contrast, the MoS₂ multilayer has an indirect bandgap of 1.3 eV and a direct bandgap of 1.8 eV with vacancy states. These variables show gap energy (exciton transition energy or bandgap or E_{11}), such as a vacancy peak energy (mid-gap energy) of 1.7 eV. Following the reduction of layers to a monolayer, there is a transition between the indirect band gap and direct gap. For this reason, there is plenty of room to control the energy gap layer-by-layer with the HIM treatment.

The conductivity of the MoS₂ before and after HIM

To illustrate the effect of the ion beam on the energy band of the sample, angle-resolved photoemission spectroscopy (ARPES) is necessary, as shown in Fig. 2a, b before and after ion treatment, respectively. Clearly, the top of the valence band of the treated sample increases by 0.5 eV, which indicates that the treated sample is likely to change from an n-type semiconductor to a p-type semiconductor. The result is consistent with the theoretical calculations in Fig. 1b. XPS analysis was also used to show the change in Mo_{3d} and S_{2p} before and after ion beam processing, as shown in Fig. 2c, d. With increasing sputter time, the binding energy and main peak intensity of Mo_{3d} and S_{2p} all show a downward trend. The reduced binding energy indicates that the valence band electrons of the sample are more likely to escape, indicating that the valence band top is rising. Note that the intensity of the main peaks of both are decreasing, but the intensity of S_{2p} decreases less than Mo_{3d} from 5 minutes from the start of sputtering, and the decrease in the S_{2p} intensity is greater than Mo_{3d} from 5 minutes to 20 minutes. This shows that at the early stage of vacancy generation, the loss of Mo is more than that of S because Mo is much heavier than other atoms such as He and S, and then, the loss of S will be more than that of Mo afterwards.

As shown in Fig. 2e, f, the IV characteristics indicate that the structural vacancies induced by HIM can act as scatter centers in the channel, resulting in a reduced drain current both in the monolayer and multilayer field effect transistors (FETs). The on/off ratio of the monolayer and multilayer MoS₂ were about 10³ and 10⁴ in Fig. 2e, f, both before and after treated. In Fig. 2e, f, the IV characteristics show an approximately linear interval from 10 V to calculate and obtain the results of 9/16 and 2/5(monolayer and multilayer) to 15 V, where we can estimate the mobility of these devices from $\mu = (L/W)\,(dI/dV_g)\,(1/CV_d)$[7]. In this equation, L is the device length, W is the device width and C is the back gate capacitance (the back gate capacitance can be estimated by $\varepsilon A/t_{ox}$, where ε is the dielectric constant of SiO₂, A is the effective area of the back gate and t_{ox} is the thickness of SiO₂). According to the equation, the mobility decreases slightly after HIM treatment of the monolayer and multilayer. In other words, the monolayer and multilayer MoS₂ treated by HIM kept their conductivity in the FET, and the HIM is a gentle way to treat the 2D devices. This phenomenons can be attributed to scattering due to vacancies, the shift of band, or both.

The magnetic property of the treated MoS₂

The magnetism of the materials can be explained by magnetic moment theory. Atomic magnetic moments are divided into orbital magnetic moments, spin magnetic moments and nuclear magnetic moments. In practice, nuclear magnetism can often be neglected in solids. In the shell filled with electrons, the orbital and spin angular momentum of each electron cancel each other out so that the total angular momentum and the total magnetic moment are zero. Only unpaired electron magnetic moments in the unfilled shell contribute to the total magnetic moment of the atom. Hence, the key to vacancy modulation of the MoS₂ monolayer is to create unpaired electrons to obtain local magnetic moments.

Due to the complexity of the sandwich structure and the binary element system involved, MoS₂ monolayers have various types of vacancies and complicated vacancy formation mechanisms. Abundant vacancies inevitably exist in the MoS₂ monolayer grown by chemical vapor deposition (CVD), which is suggested by the second law of thermodynamics. However, vacancies are often unintentionally generated using CVD. To control the type and density of vacancies, the ion beam irradiation method is of great use by controlling the irradiation parameters, such as the type, energy, and influence of incident ions. It is possible to control the formation of uniform S vacancies from 20% to 60% of the sample by ion beam treatment. The exfoliated pristine MoS₂ is irradiated with 3 MeV particles at controlled doses to create different densities of S vacancies. Before and after controllable He ion irradiation, the S to Mo atomic ratio is monitored using nano-Auger electron spectroscopy (nano-AES). Monte Carlo simulation
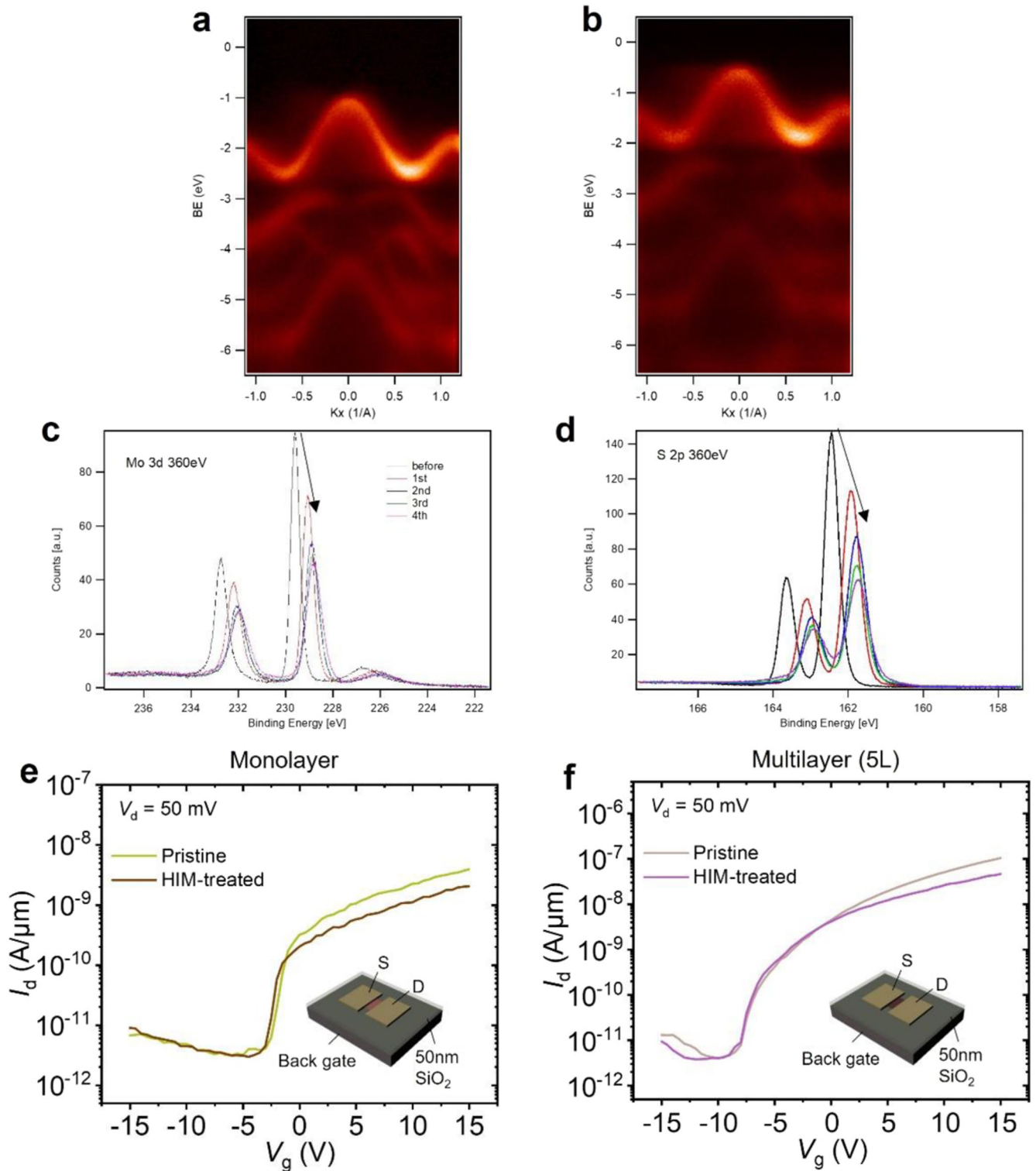
Fig. 2 ARPES spectra and XPS spectra and I-V characteristics of the samples before and after treatment. ARPES spectra of the pristine **a** and treated **b** samples. XPS spectra analysis of the Mo_{3d} **c** and S_{2p} **d** orbitals. Both show a decreasing tendency in their binding energies and intensities with increasing sputtering time. $I–V$ characteristics of the FETs made with the monolayer and multilayer (5 L) samples before **e** and after **f** treatment. The FET structures are shown in the insets of **e** and **f**. After treatment, the curves of the monolayer and multilayer samples slightly decrease, which implies reduced mobility.

is performed, and it is estimated that a 7.5×10^{23} vacancy/cm³ ion is generated on MoS₂ upon particle irradiation, which corresponds to a 6×10^{11} cm²² defect density, or approximately one defect per 100-unit cells, for an 8×10^{13} cm²² irradiation dose.

The atom Mo in MoS₂ is sandwiched between two layers of atoms S, forming a strong ligand field due to the Mo-S covalent bonds. Therefore, the magnetism of Mo atom is quenched and MoS₂ exhibits nonmagnetic. The formation of vacancies, especially
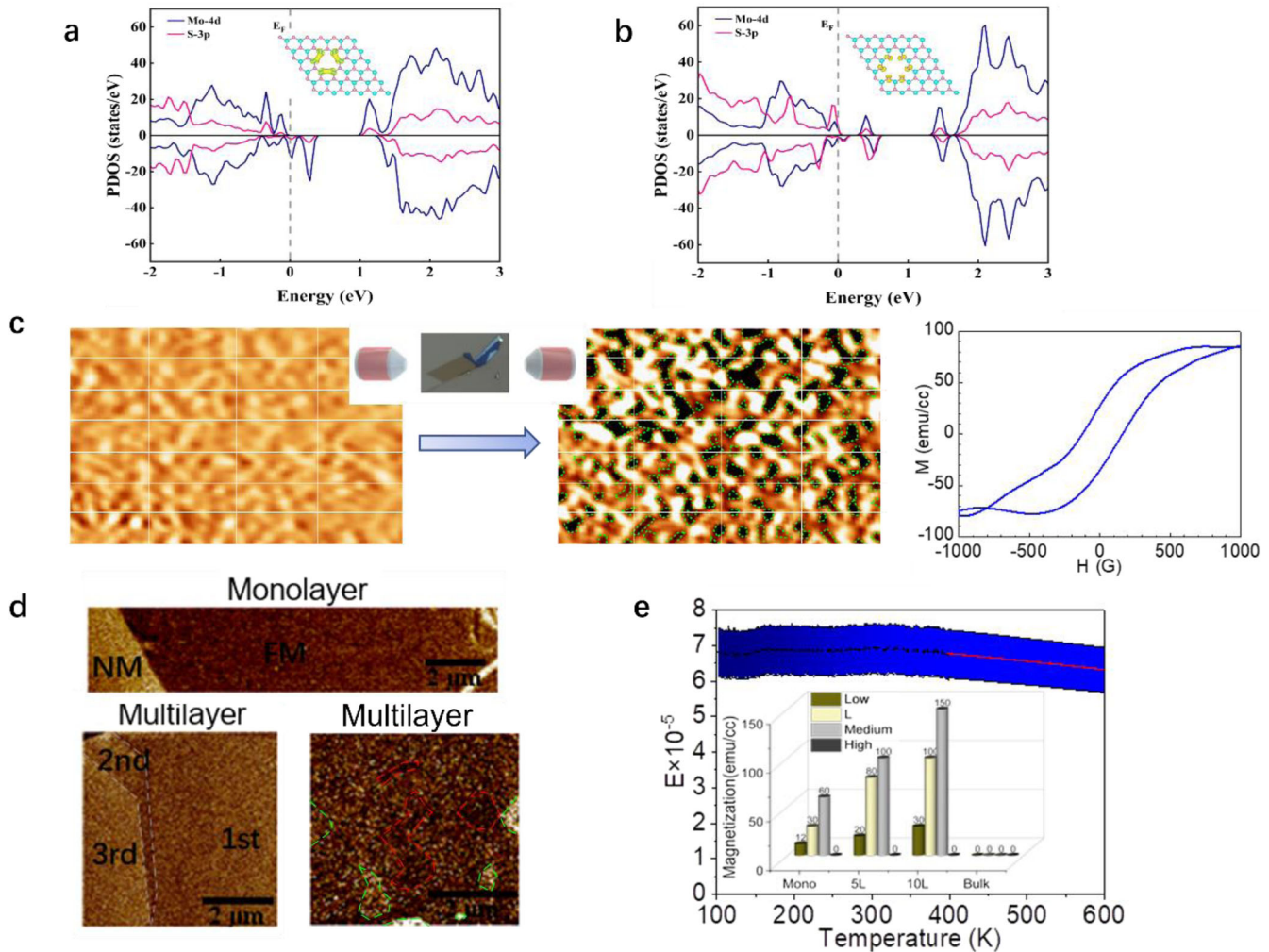
Fig. 3 Magnetic properties of the treated samples. PDOS of the *S*-edge **a** and *Mo*-edge **b** nanoholes. The red line represents the S-3p orbital, and the blue line represents the *Mo-4d* orbital. The spin densities of the two nanoholes are shown in the inset. **c** STM of the monolayer MoS$_2$ sample before (left) and after applying a magnetic field (middle). In the middle picture, the magnetic domains are framed by green dashed lines. A hysteresis loop of the multilayer is shown in c (right). The scale bar is 3 nm. **d** MFM of the monolayer and multilayer MoS$_2$ samples after treatment. In the monolayer sample, ferromagnetism and non-magnetism are clearly divided. In the multilayer sample (bottom left), three different layers are distinguished by the grey dashed line. In the multilayer sample (bottom right), different domains are framed by the red dashed line and green dashed line. **e** M-T characteristics of the multilayer MoS$_2$ sample and the relationship among the number of layers, ion dose and magnetization of MoS$_2$ (inset). Error bars of ± 10% are shown as a blue fading region. The M-T characteristics show a decreasing tendency (red line) after 320 K.

the nanohole vacancies, can greatly reduce the covalent interactions between *Mo-S* bonds. As shown in Fig. 1b, near the Fermi level, the transition density of states (TDOS) of two nanoholes is asymmetrical up and down, which means that the number of electrons in the spin-up state and spin-down state is not equal. This case will cause the structure to become magnetic. To illustrate the generation of magnetism, we performed further theoretical calculations on these two structures to obtain their spin density and projected density of states (PDOS), as shown in Fig. 3a, b and their insets. Both structures present relatively high spin state stability and ferromagnetic (FM) coupling properties. The calculated magnetic moments of the V_S-edge and V_{Mo}-edge structures are 3.9 μB and 6.0 μB, respectively. The top of Fig. 3a, b gives the spin density distribution of the V_S-edge and V_{Mo}-edge structures. Regarding the V_S-edge structure, the spin states are localized on the *S* atoms at the edge, while regarding the V_{Mo}-edge structure, the spin states are mainly concentrated on the *Mo* atoms at the edge; additionally, the three adjacent *Mo* atoms are also shown to have a small spin polarization. From the results of the PDOS, it can

be seen that in the V_S-edge structure, the spin polarization is mainly derived from the asymmetry of the S_{3p} orbitals, while in the V_{Mo}-edge structure, the asymmetry of the *Mo-4d* orbitals plays a major role. Previous studies on graphene and *h*-BN predicted that zigzag edges containing vacancies would have magnetic moments; notably, the nanoholes of monolayer MoS$_2$ result in the existence of zigzag edges[39–42]. Clearly, due to the zigzag edges containing vacancies, the S_{3p} and Mo_{4d} orbitals are not completely filled, resulting in magnetic moments on the corresponding atoms.

Experiments were performed to investigate the magnetic properties of our sample, as shown in Fig. 3. To overcome the limitation of surface volume-averaged magnetometry measurements, it is not trivial to exfoliate flake-type MoS$_2$ sheets in a range of slightly larger than tenths of microns, as shown in Fig. 1a. Two magnetometry methods are used for the samples: scanning probe microscopy (SPM, field-applied scanning tunneling microscopy) and magneto-optical Kerr effect (MOKE) magnetometry. In Fig. 3, we show the magnetic properties of MoS$_2$ through the direct
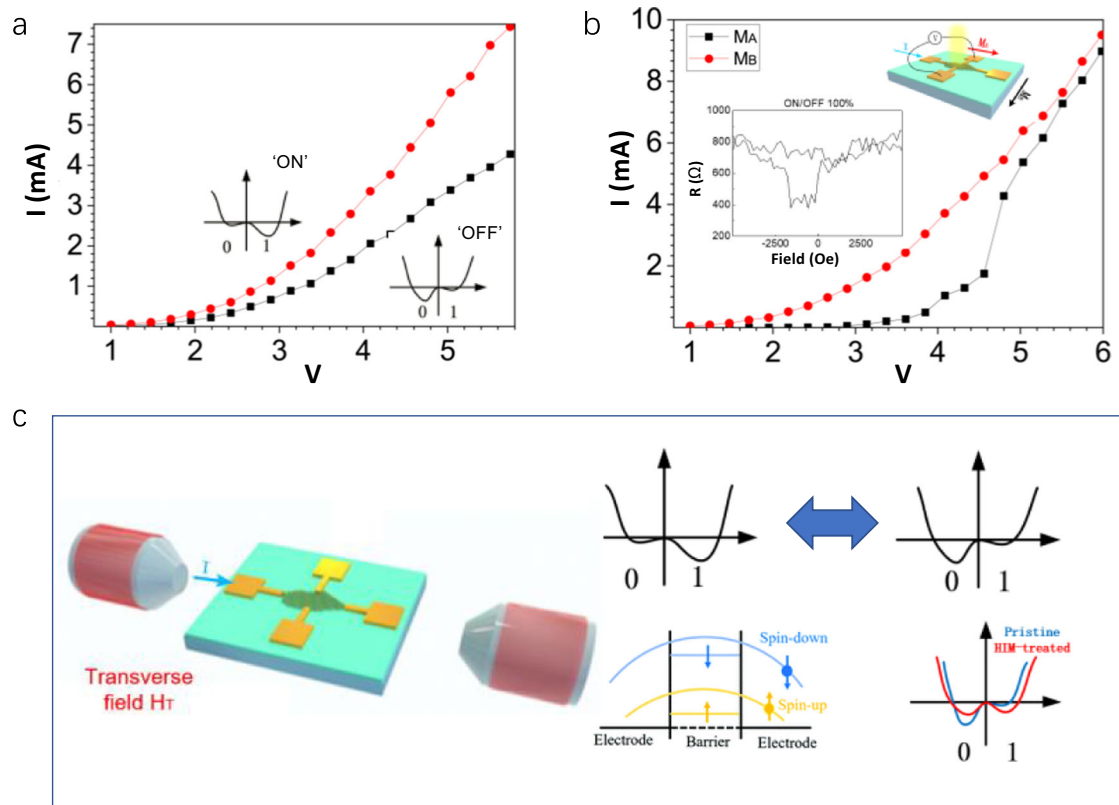
Fig. 4 Spin photocurrent characteristics. a *I–V* characteristics of the samples in dark (black line) and light (red line) situations. **b** *I–V* characteristics in the light situation when applying magnetic fields parallel (red line) and perpendicular (black line) to the current direction. A schematic of this measurement and the ON/OFF characteristics in the magnetic field are shown in the insets. The on/off ratio is more than 70%. **c** Principle of the spin filter effect at the Schottky barrier.

scanning tunnel microscopy (STM) and magnetic force microscopy (MFM) measurements and an analysis of m-H loops in a temperature range from room temperature to 500 K for several relatively large samples. It is expected that vacancies may result in unpaired electrons and consequently local magnetic moments; thus, high-density magnetism depends on the density of vacancies. Domain formation is observed by the formation of S vacancies, which break the transitional symmetry of the lattice. This leads to the creation of localized states at the Fermi level, and the states become magnetically polarized due to electron-electron interactions. When applying a magnetic field in the plane of MoS_2, domain formation can be observed. In Fig. 3c, we show the STM pictures of the treated monolayer MoS_2 before and after applying a magnetic field. Many black areas framed by the green dashed line appear after applying a magnetic field, which is evidence for the formation of a magnetic domain. In addition, a complete hysteresis loop is measured with our multilayer sample. Further experiments were performed on our sample, as shown in Fig. 3d. The MFM images show the magnetic domain structures that exist between the treated and substrate regions. Based on the experimental and theoretical calculation results, we believe that zigzag edges containing vacancy defects are generated in the monolayer after HIM treatment, thus exhibiting FM properties.

Moreover, we also captured the trace magnetism in the multilayer samples by MFM, which are framed by the red dashed line and green dashed line (Fig. 3d). Further experiments were performed to investigate the relationship among the magnetism, layer number and ion dose, and the results are shown in the inset of Fig. 3e. When the layer number is fixed and the ion dose is increased, the magnetism of the sample increases. However, a high ion dose will cause the sample to lose its magnetic

properties. The reason for this phenomenon can be explained as follows: in the case of a low dose, the more ions there are, the more vacancies that are generated; therefore, the greater the magnetism that is generated. While in the case of a high dose, the excessive ion irradiation completely destroys the surface of the sample; thus, the magnetism gradually weakens or even disappears. The relationship between the magnetism and layer number is similar to that between the magnetism and ion dose. When the ion dose is fixed and the layer number is increased, the magnetism of the sample increases. However, in the case of bulk MoS_2, no magnetic property is observed.

The domain is formed and propagated if we apply a stray field through the different MFM tips by changing their magnetic coercivity and magnetization. To understand the mechanism of switching from the magnetometry measurements, Fig. 4c illustrates the sequence of spin switching as the applied magnetic field. The magnetic moment is from the spin angular momentum of 1/2, and the protrusions represent vacancies. Vacancies and interstitials can act as very efficient traps for electrons, holes, and excitons and strongly influence the transport optical and magnetic properties of the host material. Another observation relates to the type of long-range magnetism in the samples under study. We performed MFM measurement because for the small samples, this is the most convincing experiment. This directly illustrates the drastic magnetization increase after the sample is treated. Simultaneously obtaining the AFM and MFM images also allowed for the trivial matching of the observed local magnetic properties in the targeted areas.

MOKE magnetometry was used to measure the magnetization versus temperature (T-M) in a temperature range from 100 K to 400 K. The room-temperature value of approximately 160 emu/cc

for the saturation magnetization corresponds to approximately 0.6 µB per atom. The magnetic order in MoS$_2$ can be due to the atomically controllable vacancies that have a net magnetic moment. To experimentally investigate the system, we built an ultrahigh-sensitivity MOKE setup to reduce the light scattering caused by the use of a nonuniform thin-film structure (which has periodically patterned structures) instead of continuously blanketed thin-film structures.

A MoS$_2$ spin device

Figure 4 shows the photocurrent and device function based on light emission (on/off) and magnetic field (on/off). Figure 4a shows ordinary photocurrent characteristics, where the red curve is the current in light and the black curve is the current in darkness. The current increases as a beam of light hits the surface of the sample. However, in Fig. 4b, abnormal characteristics appear when applying a magnetic field parallel to and perpendicular to the direction of the current under the presence of light, as described in the inset of Fig. 4b. It shows an on/off function similar to light emission. Anomalous Hall measurements were then taken because the integration of magnetic MoS$_2$ with electrodes and substrates is an essential step in device realization. To understand the interfacial properties between magnetic MoS$_2$ layers, we performed an experiment using a photocurrent.

As shown in Fig. 4c, we find a unique Schottky contact type with strongly spin-dependent barriers in magnetic MoS$_2$. This can be understood by the synergistic effects between the exchange splitting of the semiconductor band of MoS$_2$ and interlayer charge transfer. The spin asymmetry of the Schottky barriers may result in the different tunneling rates of spin-up and down electrons and then lead to a spin-polarized current, namely, the spin-filter (SF) effect. Moreover, by introducing Mo/S vacancies into MoS$_2$, an ohmic contact forms in the spin-up direction. This may enhance the transport of spin-up electrons and improve the SF effect. Our systematic study reveals the unique interfacial properties of MoS$_2$ layers based on magnetic vdW heterostructures.

We can describe the unique electronic properties of monolayer transition metal dichalcogenides (TMDs), which are two-dimensional materials with a hexagonal lattice structure. Because of the way the atoms are arranged in the lattice, electrons in these materials have an extra degree of freedom called "valley" in addition to their charge and spin. The K and K' valleys are two inequivalent points in the Brillouin zone (a mathematical construct used to describe the electronic structure of crystals) where electrons can reside[52].

The presence of time-reversal symmetry (where the momentum vector K is equivalent to its negative -K) leads to opposite signs of spin splitting between the K and K' valleys in monolayer TMDs. This is illustrated in Fig. 4c. The two energy levels corresponding to the spin-up state with a spin of $+\hbar/2$ at the K valley, denoted $|K\uparrow\rangle$, and the spin-down state with a spin of $-\hbar/2$ at the K' valley, denoted $|K'\downarrow\rangle$, are separated from the other two energy levels denoted $|K\downarrow\rangle$ and $|K'\uparrow\rangle$ by the spin-orbit coupling (SOC) energy. This SOC energy arises from the strong spin-orbit coupling of the d orbitals of the heavy metal atoms in the monolayer TMDs.

The explicit inversion symmetry breaking of the monolayer TMD crystal structure by the heavy metal atoms also breaks the lock on the spin and valley degrees of freedom. This means that electrons can be controlled and manipulated based on their spin and valley properties. These phenomena could potentially be used to create photosensitive magnetic semiconducting switches, which are devices that can be switched on and off using light and magnetic fields.

DISCUSSION

It is important and challenging for the spintronic devices to find a way to obtain the 2D ferromagnetic semiconductors at room temperature. It's best to obtain room temperature ferromagnetism and not to destroy the excellent semiconducting properties of 2D semiconductor. The HIM treatment of mechanically exfoliated MoS$_2$ proposed in the paper is a gentle and controllable physical method, which achieves the desired results, as useful and universal as for the treatment of other 2D semiconductor.

MoS$_2$ monolayers and multilayers with controllable nanoholes obtained by HIM treatment, displayed high-density room-temperature magnetism, with a saturation magnetization of 0.6 Bohr per single atom as the results calculated by the Monte Carlo method. The room temperature ferromagnetism and photosensitivity of the MoS$_2$ films with controllable nanoholes structure were characterized. The I-V curves of MoS$_2$ FET devices demonstrated that the HIM treatment preserves the semiconductor properties of MoS$_2$ well. The spin-optical switching devices with the MoS$_2$ films demonstrated the optical, electrical, and magnetic tunable multi-adjustable characteristics of the devices. Also, the device shows photosensitive magnetization switching which could be used as a light sensitive ferromagnetic semiconductor.

In conclusion, we demonstrated the interesting effect of controllable vacancies or nanoholes through HIM treatment on the semiconductivity and magnetic properties of treated MoS$_2$. The promotion of the HIM treatment needs to be done on a class of 2D materials and more wafer-level samples.

METHODS SUMMARY

Fabrication of MoS$_2$ and HIM treatment

MoS$_2$ crystals (SPI Supplies) are transferred onto Si/SiO$_2$ (260 nm thick) substrates using the micromechanical exfoliation technique. The flakes of interest consisting of mono-multilayer junctions are identified using an optical microscope. These flakes are formed naturally during the exfoliation process. In order to verify the thicknesses of the mono-multilayer regions, atomic force microscopy (AFM) is performed. Monolayer thickness of 0.7 nm is confirmed and multilayer thicknesses ranging from 6-15 nm is measured for the different samples. Photoluminescence (PL) and Raman mapping of the flakes was conducted to further depict the mono- and multi-layer regions using a 532 nm pump laser with 8–80 µW power and a spot size of ~0.5 µm (Horiba Scientific LabRAM HR 800). Metal source/drain (S/D) contacts are subsequently formed with one contact on the monolayer region and the other on the multilayer region of the MoS$_2$ flake. Electron-beam lithography was used to pattern the metal contacts, followed by evaporation of Ti/Au (100/30 nm) and lift-off of the resist in acetone.

Scanning probe microscopy

SEM images were collected with a Carl Zeiss LEO 1550 instrument. The SPM study was performed in noncontact mode using a Veeco Dimension 3100 system, and the MFM measurements were conducted in dynamic lift mode with a lift-off distance of 30 nm.

Magneto-optical Kerr spectroscopy

To perform high-resolution magneto-optical Kerr spectroscopy, we used a focused MOKE system in lateral mode. The light source was directed towards the sample, which was located between the poles of a vector magnet that could reach 400 Oe with a homemade electromagnet.

Temperature dependence measurements

The setup used for the temperature dependence measurements was critical in this experiment. The sample was mounted onto a

heater using cigarette paper and GE-7031 to withstand thermal cycling, and the thermocouple was mounted onto the sample to measure the temperature directly. A 99.999% pure indium wire was used to mount the thermocouple. The precise temperature of the sample, as measured by the heater, was carefully calibrated to reduce any unwanted thermal fluctuations in the thermal cycles during the measurements.

Photocurrent measurement

The m-H loop measurements were performed using a VSM 7400 Lake Shore Cryotronics instrument with a 3.1-T electromagnet. The sample was mounted on a quartz holder, and vacuum grease was used to permit the system to withstand the vibration cycles.

Computational methods

The electron-ion interaction is described by the projected augmented wave (PAW) method, and the Perdew-Burke-Ernzerhof (PBE) of generalized gradient approximation (GGA) is adopted for the exchange-correlation functional[53,54]. To ensure good calculation coverage, the plane-wave energy cut-off is set to 400 eV. The geometric structures are fully relaxed until the force acting on each atom is less than 0.01 eV/A and the electronic iteration energy convergence criterion is 10^{-6} eV. A $6 \times 6 \times 1$ MoS_2 supercell, which relates to a $6 \times 6 \times 1$ gamma centered k-point mesh, is used to model the vacancy defect.

DATA AVAILABILITY

All data are available in the main text or the supplementary materials.

REFERENCES

1. Ieong, M., Doris, B., Kedzierski, J., Rim, K. & Yang, M. Silicon device scaling to the sub-10-nm regime. *Science* **306**, 2057–2060 (2004).
2. Hei, W. & Hiroshi, I. The road to miniaturization. *Physics World* **18**, 40 (2005).
3. Wolf, S. A. et al. Spintronics: a spin-based electronics vision for the future. *Science* **294**, 1488–1495 (2001).
4. Hirohata, A. & Takanashi, K. Future perspectives for spintronic devices. *J. Phys. D: Appl. Phys.* **47**, 193001 (2014).
5. Gong, C. & Zhang, X. Two-dimensional magnetic crystals and emergent heterostructure devices. *Science* **363**, eaav4450 (2019).
6. Ahn, E. C. 2D materials for spintronic devices. *npj 2D Mater. Appl.* **4**, 17 (2020).
7. Feng, Y. P. et al. Prospects of spintronics based on 2D materials. *Wiley Interdiscip. Rev.: Comput. Mol. Sci.* **7**, e1313 (2017).
8. Gibertini, M., Koperski, M., Morpurgo, A. F. & Novoselov, K. S. Magnetic 2D materials and heterostructures. *Nat. Nanotechnol.* **14**, 408–419 (2019).
9. Mak, K. F., Shan, J. & Ralph, D. C. Probing and controlling magnetic states in 2D layered magnetic materials. *Nat. Rev. Phys.* **1**, 646–661 (2019).
10. Dai, C. et al. Research progress of two-dimensional magnetic materials. *Sci. China Mater.* **66**, 859–876 (2023).
11. Liu, W. et al. A room-temperature magnetic semiconductor from a ferromagnetic metallic glass. *Nat. Commun.* **7**, 13497 (2016).
12. Hossain, M., Qin, B., Li, B. & Duan, X. Synthesis, characterization, properties and applications of two-dimensional magnetic materials. *Nano Today* **42**, 101338 (2022).
13. Dąbrowski, M. et al. All-optical control of spin in a 2D van der Waals magnet. *Nat. Commun.* **13**, 5976 (2022).
14. Meseguer-Sánchez, J. et al. Coexistence of structural and magnetic phases in van der Waals magnet CrI$_3$. *Nat. Commun.* **12**, 6265 (2021).
15. Patil, R. A. et al. Intriguing field-effect-transistor performance of two-dimensional layered and crystalline CrI$_3$. Materials Today. *Mater. Today Phys.* **12**, 100174 (2020).
16. Wines, D., Choudhary, K. & Tavazza, F. Systematic DFT+U and quantum Monte Carlo benchmark of magnetic two-dimensional (2D) CrX$_3$ (X= I, Br, Cl, F). The. *J. Phys. Chem. C* **127**, 1176–1188 (2023).
17. Zhao, Y., Guo, Y., Zhou, S. & Zhao, J. XGT (X= Fe, Mn, Cr; G= Ge; T= Te): A family of two-dimensional ternary intrinsic magnetic materials. *Phys.Rev. Mater.* **6**, 044005 (2022).
18. Birch, M. T. et al. History-dependent domain and skyrmion formation in 2D van der Waals magnet Fe$_3$GeTe$_2$. *Nat. Commun.* **13**, 3035 (2022).
19. Lin, M. W. et al. Ultrathin nanosheets of CrSiTe$_3$: a semiconducting two-dimensional ferromagnetic material. *J. Mater. Chem. C* **4**, 315–322 (2016).
20. Ahmad, H. et al. S-band Mode-locked Thulium-doped fluoride fiber laser using FePS$_3$ as saturable absorber. *Opt. Fiber Technol.* **72**, 102985 (2022).
21. Mertens, F. et al. Ultrafast coherent the lattice dynamics coupled to spins in the van der Waals antiferromagnet FePS$_3$. *Adv. Mater.* **35**, 2208355 (2023).
22. Martín-Pérez, L. et al. Direct magnetic evidence, functionalization, and low-temperature magneto-electron transport in liquid-phase exfoliated FePS$_3$. *ACS nano* **17**, 3007–3018 (2023).
23. Lee, Y. et al. Giant magnetic anisotropy in the atomically thin van der Waals antiferromagnet FePS$_3$. *Adv. Electron. Mater.* **9**, 2200650 (2023).
24. Bera, A., & Sood, A. K. *MoS$_2$: Materials, Physics, and Devices*. (Springer International Publishing, 2014).
25. Sangwan, V. K. et al. Multi-terminal memtransistors from polycrystalline monolayer molybdenum disulfide. *Nature* **554**, 500–504 (2018).
26. Tang, J. et al. Low power flexible monolayer MoS$_2$ integrated circuits. *Nat. Commun.* **14**, 3633 (2023).
27. Manzeli, S., Ovchinnikov, D., Pasquier, D., Yazyev, O. V. & Kis, A. 2D transition metal dichalcogenides. *Nat. Rev. Mater.* **2**, 1–15 (2017).
28. Li, S. L., Tsukagoshi, K., Orgiu, E. & Samorì, P. Charge transport and mobility engineering in two-dimensional transition metal chalcogenide semiconductors. *Chem. Soc. Rev.* **45**, 118–151 (2016).
29. Kim, M. et al. Monolayer molybdenum disulfide switches for 6G communication systems. *Nat. Electron.* **5**, 367–373 (2022).
30. Zhou, Y., Yang, P., Zu, H., Gao, F. & Zu, X. Electronic structures and magnetic properties of MoS$_2$ nanostructures: atomic defects, nanoholes, nanodots and antidots. *Phys. Chem. Chem. Phys.* **15**, 10385–10394 (2013).
31. Nan, H. et al. Strong photoluminescence enhancement of MoS$_2$ through defect engineering and oxygen bonding. *ACS nano* **8**, 5738–5745 (2014).
32. Sakong, W. et al. Optical duality of molybdenum disulfide: metal and semi-conductor. *Nano Lett.* **22**, 5207–5213 (2022).
33. Krane, N., Lotze, C., Läger, J. M., Reecht, G. & Franke, K. J. Electronic structure and luminescence of quasi-freestanding MoS$_2$ nanopatches on Au (111). *Nano Lett.* **16**, 5163–5168 (2016).
34. Tongay, S. et al. Defects activated photoluminescence in two-dimensional semiconductors: interplay between bound, charged and free excitons. *Sci. Rep.* **3**, 2657 (2013).
35. Garcia-Esparza, A. T. et al. Local structure of sulfur vacancies on the basal plane of monolayer MoS$_2$. *ACS nano* **16**, 6725–6733 (2022).
36. Eginligil, M. et al. Dichroic spin–valley photocurrent in monolayer molybdenum disulphide. *Nat. Commun.* **6**, 7636 (2015).
37. Kang, M. et al. Universal mechanism of band-gap engineering in transition-metal dichalcogenides. *Nano Lett.* **17**, 1610–1615 (2017).
38. Cao, T. et al. Valley-selective circular dichroism of monolayer molybdenum disulphide. *Naturecommunications* **3**, 887 (2012).
39. Tongay, S., Varnoosfaderani, S. S., Appleton, B. R., Wu, J. & Hebard, A. F. Magnetic properties of MoS$_2$: Existence of ferromagnetism. *Appl. Phys. Lett.* **101**, 123105 (2012).
40. Jie, W. et al. Observation of room-temperature magnetoresistance in monolayer MoS$_2$ by ferromagnetic gating. *ACS Nano* **11**, 6950–6958 (2017).
41. Cai, L. et al. Vacancy-induced ferromagnetism of MoS$_2$ nanosheets. *J. Am. Chem. Soc.* **137**, 2622–2627 (2015).
42. Xiang, Z. et al. Room-temperature ferromagnetism in Co doped MoS$_2$ sheets. *Phys. Chem. Chem. Phys.* **17**, 15822–15828 (2015).
43. Mak, K. F., McGill, K. L., Park, J. & McEuen, P. L. The valley Hall effect in MoS$_2$ transistors. *Science* **344**, 1489–1492 (2014).
44. Mak, K. F., Lee, C., Hone, J., Shan, J. & Heinz, T. F. Atomically thin MoS$_2$: a new direct-gap semiconductor. *Phys. Rev. Lett.* **105**, 136805 (2010).
45. Pan, H. & Zhang, Y. W. Tuning the electronic and magnetic properties of MoS$_2$ nanoribbons by strain engineering. *J. Phys. Chem. C* **116**, 11752–11757 (2012).
46. Lu, J. M. et al. Evidence for two-dimensional Ising superconductivity in gated MoS$_2$. *Science* **350**, 1353–1357 (2015).
47. Conley, H. J. et al. Bandgap engineering of strained monolayer and bilayer MoS$_2$. *Nano Lett.* **13**, 3626–3630 (2013).
48. Burch, K. S., Mandrus, D. & Park, J. G. Magnetism in two-dimensional van der Waals materials. *Nature* **563**, 47–52 (2018).
49. Zhao, G. Y. et al. Recent progress on irradiation-induced defect engineering of two-dimensional 2H-MoS$_2$ few layers. *Appl. Sci.* **9**, 678 (2019).
50. Nguyen, V. L. et al. Wafer-scale integration of transition metal dichalcogenide field-effect transistors using adhesion lithography. *Nat. Electron.* **6**, 146–153 (2023).

51. Klein, J. et al. Robust valley polarization of helium ion modified atomically thin MoS$_2$. *2D Mater.* **5**, 011007 (2018).

52. Xu, X. et al. Spin and pseudospins in layered transition metal dichalcogenides. *Nat. Phys.* **10**, 343–350 (2014).

53. Perdew, J. P., Burke, K. & Ernzerhof, M. Generalized gradient approximation made simple. *Phys. Rev. Lett.* **77**, 3865 (1996).

54. Kresse, G. & Joubert, D. From ultrasoft pseudopotentials to the projector augmented-wave method. *Phys. Rev. B* **59**, 1758 (1999).

ACKNOWLEDGEMENTS

AUTHOR CONTRIBUTIONS

J.L. and J.H. wrote the main manuscript text and J.C., J.L., and J.H. prepared Figs. 1–4. All authors reviewed the manuscript. J.H. conceived the idea of this project. J.H., J.C. and Y.X. prepared the samples and obtained the experiment data. C.Z. and H.S. conducted the simulation part. J.L. and P.Z. analyzed the data with input from J.H. who also supervised the project. All authors discussed the results. J.H. and J.L. wrote the manuscript with the contributions from all authors.

COMPETING INTERESTS

The authors declare no competing interests.

ADDITIONAL INFORMATION

Supplementary information The online version contains supplementary material available at https://doi.org/10.1038/s44306-024-00009-4.

Correspondence and requests for materials should be addressed to Jeongmin Hong.

Reprints and permission information is available at http://www.nature.com/reprints

Publisher's note Springer Nature remains neutral with regard to jurisdictional claims in published maps and institutional affiliations.